

## NUMERICAL PREDICTION OF THE TRANSITIONAL FLOW PAST POWER-LAW LEADING EDGES

**Wilson F. N. Santos**

Combustion and Propulsion Laboratory  
National Institute for Space Research  
12630-000 Cachoeira Paulista, SP, Brazil  
[wilson@lcp.inpe.br](mailto:wilson@lcp.inpe.br)

**Abstract.** *This work deals with a numerical study of power-law shaped leading edges situated in a hypersonic flow at zero-incidence. The primary aim of this paper is to examine the effect of rarefaction on the flowfield structure. Rarefaction effect on the flowfield structure has been investigated by employing the Direct Simulation Monte Carlo (DSMC) method. The work is motivated by interest in investigating power-law shaped leading edges as possible candidates for blunting geometry of hypersonic leading edges. The sensitivity of the primary flow properties to variations on rarefaction is simulated for altitudes of 70, 80 and 85 km. The analysis shows significant differences on the flowfield properties due to variations not only on the altitude but also on the leading edge shape defined by the power-law exponent. It is found that the upstream effects have different influence on velocity, density, pressure and temperature along the stagnation streamline ahead of the leading edges.*

**Keywords.** *DSMC, hypersonic flow, rarefied flow, power-law shape, sharp leading edge.*

### 1. Introduction

Hypersonic waverider configurations have been proposed as promising airframes for high-speed vehicles because they have the highest known lift-drag (L/D) performance. A waverider concept, introduced by Nonweiler (1959), is a lifting body that is derived from a known analytical flowfield, such as a flow over a two-dimensional wedge or a flow over a slender cone. The potential for high L/D ratio on waveriders originates from the high-pressure region between the shock wave and the lower surface. Due to the sharp leading edge, the attached shock wave prevents the high-pressure gas from the lower surface to communicate with the gas on the upper surface. However, as any practical waverider will have some degree of leading edge bluntness for heat transfer, manufacturing and handling concerns, then the predicted performance of waverider configurations may not be achieved. Moreover, because of the viscous effects, the shock wave will be detached from the leading edge and, hence, the aerodynamic performance of the vehicle may be degraded from ideal performance. Typically, a round leading edge with constant radius of curvature near the stagnation point (circular cylinder) has been chosen. Nevertheless, shock detachment distance on a cylinder, with associated leakage, scales with the radius of curvature. Therefore, designing a hypersonic vehicle leading edge involves a tradeoff between making the leading edge sharp enough to obtain acceptable aerodynamic and propulsion efficiency and blunt enough to reduce the aerodynamic heating in the stagnation region.

Certain classes of non-circular shapes, such as power-law shaped leading edges ( $y \propto x^n$ ,  $0 < n < 1$ ), may provide the required bluntness for heat transfer, manufacturing and handling concerns with reduced departures from ideal aerodynamic performance. This concept is based on work of Mason and Lee (1994), who have pointed out, based on Newtonian flow analysis, that power-law shapes exhibit both blunt and sharp aerodynamic properties. They suggested the possibility of a difference between shapes that are geometrically sharp and shapes that behave aerodynamically as if they were sharp.

Santos and Lewis (2002) have investigated the sensitivity of the pressure gradient and the stagnation point heating to shape variations of power-law leading edges by considering two-dimensional rarefied hypersonic flow. Through the use of the DSMC method, they showed that the pressure gradient on the power-law shapes is in surprising agreement with that obtained by Mason and Lee (1994) by employing Newtonian Analysis. They also found that the stagnation point heating scales inversely with the square root of the curvature radius for power-law bodies with finite radius of curvature.

Santos and Lewis (2005a and 2005b) compared power-law shapes to a corresponding circular cylinder in order to determine which geometry would be better suited as a blunting profile. Their analysis also showed that power-law shapes provided smaller total drag than circular cylinder, typically used in blunting sharp leading edges for heat transfer considerations. However, circular cylinder provided smaller stagnation point heating than power-law shapes under the range of conditions investigated.

Based on recent interest in hypersonic waveriders for high-altitude/low-density applications (Anderson, 1990, Potter and Rockaway, 1994, Rault, 1994, Graves and Argrow, 2001, Shvets et al., 2005), the present account deals with a parametric study performed on power-law shapes with emphasis placed on the rarefaction effects. In this context, the primary goal of this paper is to assess the sensitivity of the primary flow properties to variations not only on the rarefaction experienced by the leading edges but also on the leading-edge shapes by means of the power-law exponent.

For the high altitude/high Knudsen number of interest ( $Kn > 0.1$ ), the flowfield is sufficiently rarefied that continuum method becomes inappropriate. Alternatively, the DSMC method is used in the current study to calculate the rarefied hypersonic two-dimensional flow on the leading edge shapes.

## 2. Leading Edge Geometry Definition

In dimensional form, the body power-law shapes (Santos and Lewis, 2002) are given by the following expression,

$$y = ax^n \quad (1)$$

where  $n$  is the power-law exponent and  $a$  is the power-law constant which is a function of  $n$ .

The power-law shapes are modeled by assuming a sharp leading edge of half angle  $\theta$  with a circular cylinder of radius  $R$  inscribed tangent to this wedge. The power-law shapes, inscribed between the wedge and the cylinder, are also tangent to them at the same common point where they have the same slope angle. The circular cylinder diameter provides a reference for the amount of blunting desired on the leading edges. It was assumed a leading edge half angle of 10 degrees, a circular cylinder diameter of  $10^{-2}$ m and power-law exponents of 1/2, 2/3, and 3/4. Figure (1a) illustrates schematically this construction for the set of power-law leading edges investigated.

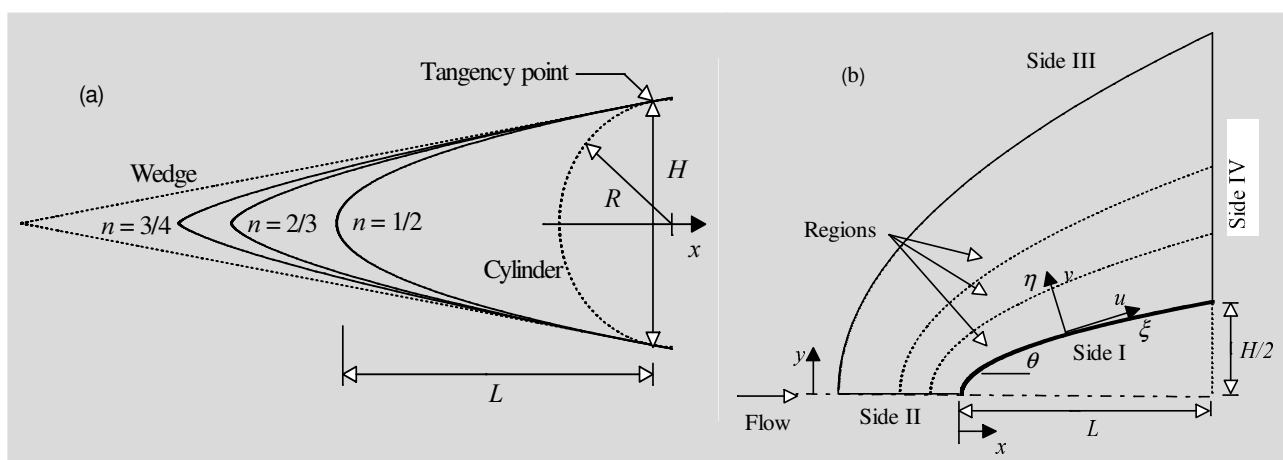


Figure 1: Drawing illustrating (a) the leading edge shapes and (b) the computational domain.

From geometric considerations, the power-law constant  $a$  is obtained by matching slope on the wedge, circular cylinder and power-law body at the tangency point. The common body height  $H$  at the tangency point is equal to  $2R\cos\theta$ , and the body length  $L$  from the nose to the tangency point in the axis of symmetry is given by  $nH/2\tan\theta$ . It was assumed that the power-law leading edges are infinitely long but only the length  $L$  is considered since the wake region behind the power-law bodies is not of interest in this investigation.

## 3. Computational Method and Procedure

The most successful numerical technique for modeling complex transitional flows has been the Direct Simulation Monte Carlo (DSMC) method (Bird, 1994). The DSMC method simulates real gas flows with various physical processes by means of a huge number of modeling particles; each particle represents a fixed number of real gas molecules. In the DSMC model, the particle evolution is divided into two independent phases during the simulation; the movement phase and the collision phase. In the movement phase, all particles are moved over distances appropriate to a short time interval, time step, and some of them interact with the domain boundaries in this time interval. Particles that strike the solid wall would reflect according to the appropriate gas-surface interaction model, specular, diffusive or a combination of these. In the collision phase, intermolecular collisions are performed according to the theory of probability without time being consumed. In this context, the intermolecular collisions are uncoupled to the translational molecular motion over the time step used to advance the simulation. Time is advanced in discrete steps such that each step is small in comparison with the mean collision time. The simulation is always calculated as unsteady flow. However, a steady flow solution is obtained as the large time state of the simulation.

The molecular collisions are modeled using the variable hard sphere (VHS) molecular model (Bird, 1981) and the no time counter (NTC) collision sampling technique (Bird, 1989). The energy exchange between kinetic and internal modes is controlled by the Borgnakke-Larsen statistical model (Borgnakke and Larsen, 1975). Simulations are performed using a non-reacting gas model consisting of two chemical species,  $N_2$  and  $O_2$ . Energy exchanges between

the translational and internal modes, rotational and vibrational, are considered. Relaxation collision numbers of 5 and 50 were used for the calculations of rotation and vibration, respectively.

In order to easily account for particle-particle collisions, the flowfield is divided into an arbitrary number of regions, which are subdivided into computational cells. The cells are further subdivided into subcells. The cell provides a convenient reference sampling of the macroscopic gas properties, while the collision partners are selected from the same subcell for the establishment of the collision rate.

The computational domain used for the calculation is made large enough so that body disturbances do not reach the upstream and side boundaries, where freestream conditions are specified. A schematic view of the computational domain is depicted in Fig. (1b). Side I is defined by the body surface. Diffuse reflection with complete thermal accommodation is the condition applied to this side. Advantage of the flow symmetry is taken into account, and molecular simulation is applied to one-half of a full configuration. Thus, side II is a plane of symmetry. In such a boundary, all flow gradients normal to the plane are zero. At the molecular level, this plane is equivalent to a specular reflecting boundary. Side III is the freestream side through which simulated molecules enter and exit. Finally, the flow at the downstream outflow boundary, side IV, is predominantly supersonic and vacuum condition is specified (Guo and Liaw, 2001). At this boundary, simulated molecules can only exit.

Application of a numerical method to solve practical problems requires a reliable way in order to estimate the accuracy of the solution. The numerical accuracy in DSMC method depends on the cell size chosen, on the time step as well as on the number of particles per computational cell. In the DSMC algorithm, the linear dimensions of the cells should be small in comparison with the scale length of the macroscopic flow gradients normal to streamwise directions, which means that the cell dimensions should be of the order of or smaller than the local mean free path (Alexander et al., 1998 and Alexander et al., 2000). The time step should be chosen to be sufficiently small in comparison with the local mean collision time (Garcia and Wagner, 2000, and Hadjiconstantinou, 2000). In general, the total simulation time, discretized into time steps, is identified with the physical time of the real flow. Finally, the number of simulated particles has to be large enough to make statistical correlations between particles insignificant.

These effects were investigated in order to determine the number of cells and the number of particles required to achieve grid independence solutions. Grid independence was tested by running the calculations with half and double the number of cells in  $\xi$  and  $\eta$  directions (see Fig. (1b)) compared to a standard grid. Solutions (not shown) were near identical for all grids used and were considered fully grid independent. Details on the grid independence effect are shown in Santos and Lewis (2005a and 2005b).

#### 4. Freestream and Flow Conditions

Rarefaction effects are investigated for altitudes of 70, 80 and 85 km. For each one of the altitude investigated, the freestream Mach number  $M_\infty$  and the wall temperature  $T_w$  are kept to the constant values of 12 and 880 K, respectively. Freestream Mach number  $M_\infty$  of 12 corresponds to freestream velocity  $V_\infty$  of 3.56, 3.236 and 3.236 km/s for altitudes of 70, 80 and 85 km, respectively.

Table (1) summarizes the freestream and flow conditions used in the present calculations. The gas properties considered in the simulation are those given by Bird (1994) and tabulated in Tab. (2). Referring to Tab. (1),  $T_\infty$ ,  $p_\infty$ ,  $\rho_\infty$ ,  $n_\infty$ ,  $\mu_\infty$  and  $\lambda_\infty$  stand respectively for temperature, pressure, density, number density, viscosity and mean free path.

Table 1: Freestream Conditions

Altitude (km)	$T_\infty$ (K)	$p_\infty$ (N/m <sup>2</sup> )	$\rho_\infty \times 10^5$ (kg/m <sup>3</sup> )	$n_\infty \times 10^{20}$ (m <sup>-3</sup> )	$\mu_\infty \times 10^5$ (Ns/m <sup>2</sup> )	$\lambda_\infty \times 10^3$ (m)	$V_\infty$ (m/s)
70	220.0	5.582	8.753	18.2090	1.455	0.903	3560
80	181.0	1.040	1.999	4.1586	1.253	3.960	3236
85	181.0	0.414	0.796	1.6550	1.253	9.940	3236

Table 2: Gas Properties

	$X$ Mole fraction	$m$ (kg) Molecular mass	$d$ (m) Molecular diameter	$\omega$ Viscosity index
O <sub>2</sub>	0.237	$5.312 \times 10^{-26}$	$4.01 \times 10^{-10}$	0.77
N <sub>2</sub>	0.763	$4.65 \times 10^{-26}$	$4.11 \times 10^{-10}$	0.74

The overall Knudsen number  $Kn_\infty$ , defined as the ratio of the freestream mean free path  $\lambda_\infty$  to the diameter of the circular cylinder, corresponds to 0.0903, 0.3960 and 0.9940 for altitudes of 70, 80 and 85 km, respectively. Finally, the Reynolds number  $Re_\infty$  per unit of meter, based on conditions in the undisturbed stream is 21416.3, 5165 and 2055 for altitudes of 70, 80 and 85 km, respectively.

## 4. Computational Results and Discussion

The regime of intermediate Knudsen numbers ( $0.1 < Kn < 10$ ), which is difficult to treat analytically, is simulated in the present account by  $Kn_\infty$  of 0.0903, 0.3960 and 0.9940, which correspond to the altitudes of 70, 80 and 85 km, respectively. These freestream Knudsen numbers were obtained by considering the diameter of the reference circular cylinder as the characteristic length. In order to assess the dependence of the flowfield structure on the freestream Knudsen number, by way of changing the altitude, the other flow parameters were kept the same as defined in Tab. (1), i.e., freestream Mach number of 12, wall temperature of 880 K, and diffuse reflection with full thermal accommodation. In this way, the purpose of this section is to discuss and to compare differences in the flowfield properties due to variations on the freestream Knudsen number as well as on the leading-edge shape. The flowfield properties of particular interest in the regime of intermediate Knudsen number are velocity, density, pressure and temperature.

### 4.1. Velocity Profile

Normal velocity profiles along the stagnation streamline and their dependence on rarefaction are illustrated in Figs. (2a), (2b) and (2c) for leading-edge shapes corresponding to power-law exponent  $n$  of 1/2, 2/3 and 3/4, respectively. In this set of figures, the normal velocity  $v$  is normalized by the freestream velocity  $V_\infty$ , which is slightly different for each altitude, and the distance  $x$  upstream the leading edges is normalized by the radius  $R$  of the reference circular cylinder instead of the freestream mean free path  $\lambda_\infty$ , since it is different for the altitudes investigated. In addition, in order to emphasize points of interest, this set of figures shows only part of the computational domain of the normal velocity profiles for altitudes of 80 and 85 km.

According to these figures, it is seen that the leading-edge shape as well as the rarefaction influences the flowfield far upstream. This domain of influence increases with increasing both the power-law exponent  $n$  and the altitude. By means of the power-law exponent  $n$ , the leading-edge shape effect results from the upstream diffusion of particles that are reflected from the nose of the leading edges. Consequently, blunting the nose of the body ( $n \rightarrow 1/2$ ) leads to larger disturbance upstream of the body. On the other hand, the effect of increasing the altitude is to create a more rarefied situation. In this fashion, the presence of the body, propagated by random motion of the molecules, is communicated to a larger distance ahead of the body, since the molecules interact little with each other and collisions among them are less frequent. For comparison purpose, the upstream disturbance for a velocity reduction of 1% ( $v/V_\infty = 0.99$ ) is around  $0.95R$ ,  $0.60R$  and  $0.54R$  for cases  $n = 1/2$ ,  $2/3$  and  $3/4$ , respectively, at an altitude of 70 km. Nevertheless, it changes to around  $5.47R$ ,  $5.00R$  and  $4.56R$  for cases  $n = 1/2$ ,  $2/3$  and  $3/4$ , respectively, at an altitude of 85 km.

Despite the large upstream influence of the altitude as well as the shape of the leading edge on the normal velocity, the significant reduction in the normal velocity takes place in a small region very close to the stagnation point. As a reference, for altitudes of 70, 80 and 85 km, a reduction of 50% in the normal velocity occurs for the  $n = 1/2$  case around  $x/R = 0.22$ ,  $0.52$  and  $0.84$ , and for the  $n = 3/4$  case around  $x/R = 0.07$ ,  $0.17$  and  $0.29$ , respectively.

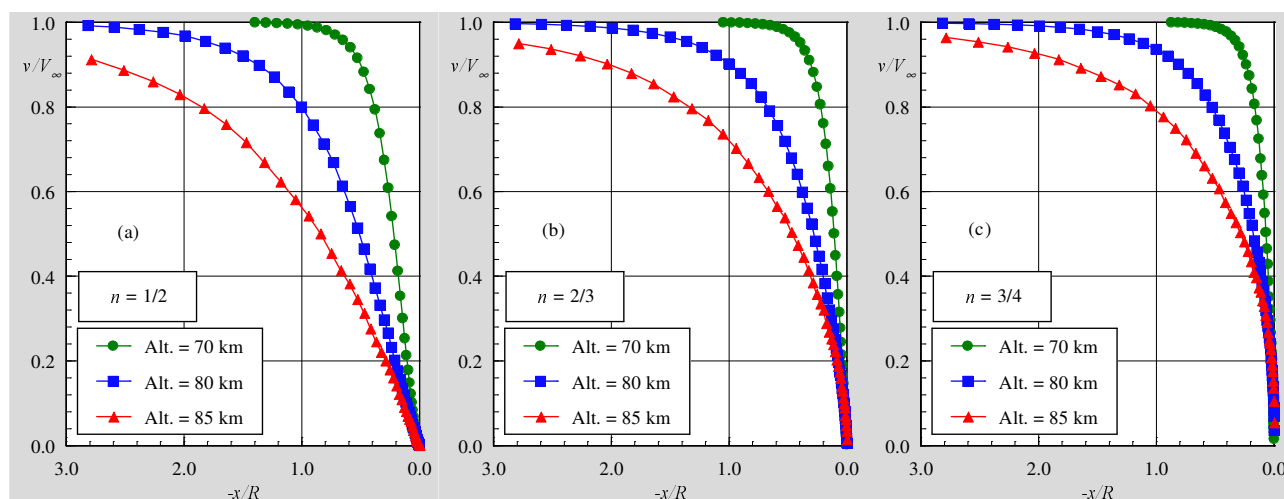


Figure 2: Normal velocity ( $v/V_\infty$ ) profiles along the stagnation streamline as a function of the altitude for leading-edge shape corresponding to power-law exponent  $n$  of (a) 1/2, (b) 2/3 and (c) 3/4.

### 4.2. Density Profile

Rarefaction effects on density along the stagnation streamline are shown as a function of the altitude in Figs. (3a), (3b) and (3c) for power-law exponent  $n$  of 1/2, 2/3 and 3/4, respectively. In this set of figures, the density  $\rho$  is normalized by the freestream density  $\rho_\infty$ , which is different for each altitude as shown in Tab. (1).

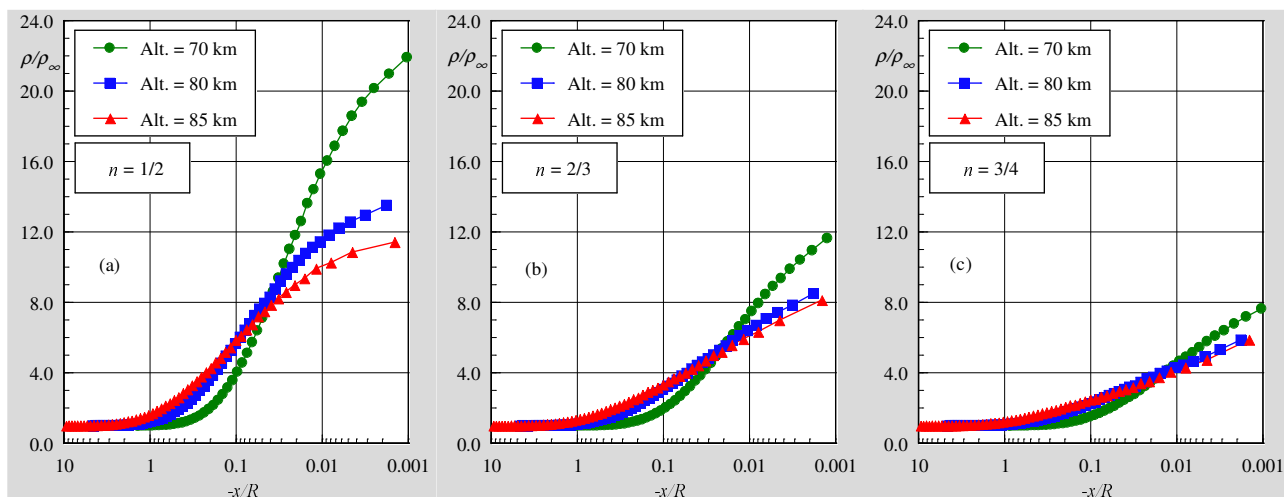


Figure 3: Density ( $\rho/\rho_\infty$ ) profiles along the stagnation streamline as a function of the altitude for leading-edge shape corresponding to power-law exponent  $n$  of (a) 1/2, (b) 2/3 and (c) 3/4.

The predictions of density for all of the leading-edge shapes investigated show no sign of a discrete shock wave. Instead, there is a continuous rise in density from the freestream to the nose of the leading edges, rising to well above the continuum inviscid limit for the majority of the cases investigated. As a point of reference, the Rankine-Hugoniot relations give a postshock density that corresponds to the ratio  $\rho/\rho_\infty = 5.8$  for freestream Mach number of 12. Near the stagnation point ( $x/R \approx 0$ ), a substantial density increase occurs which is a characteristic of cold-wall entry flow (Haas and Fallavollita, 1994). In typical entry flow, the body surface temperature is low compared to the stagnation temperature. This leads to a steep density gradient near the body surface. For the range of altitude in the present simulation, the ratio of wall temperature to stagnation temperature is from 0.134 to 0.163, which correspond to a cold-wall flow.

Referring to Figs. (3a), (3b) and (3c), it can be recognized that density rises gradually as the flow approaches the nose of the leading edge, indicating the diffuse nature of the shock wave, a characteristic of highly rarefied flows. Also, density increases much more for blunt leading edge ( $n \rightarrow 1/2$ ) than that for sharp leading edge ( $n \rightarrow 3/4$ ) in the stagnation region and reaches its maximum value at the stagnation point. As a result, the buildup of particle density near the nose of the leading edge acts as a shield for the molecules coming from the undisturbed stream. The buildup of particles density at the vicinity of the stagnation point decreases as the altitude increases from 70 to 85 km. This is explained by the fact that the effect of increasing the altitude is to create a more rarefied situation, since the molecules interact little with each other and collisions among them are less frequent. In addition, with the density decrease near the stagnation point, the local mean free path increases resulting in a higher local Knudsen number.

For the flow conditions in this set of simulations, the density ratio  $\rho/\rho_\infty$  at the stagnation point by assuming free molecular flow (Bird, 1994) is found to be 9.89, 9.07 and 9.07 for altitudes of 70, 80 and 85 km, respectively. By comparing these density ratios with those presented in the Figs. (3a), (3b) and (3c), one can conclude that the flow approaches the free molecular flow near the nose of the leading edge for power-law exponent of 3/4.

It may be recognized from the density distribution that, unlike normal velocity, density has little effect on the extent of the domain of influence upstream of the body for the leading edge shapes investigated. Much of the density increase in the shock layer occurs after the temperature has reached its postshock value, as will be seen subsequently.

In the following, it proves instructive to illustrate the density behavior adjacent to the body surface. In this fashion, density ratio ( $\rho/\rho_\infty$ ) contours at the vicinity of the nose are displayed in Figs. (4a), (4b) and (4c) for power-law exponent  $n$  of 1/2, 2/3 and 3/4, respectively. In this set of contours, the half upper part of leading edge represents the distribution of density at an altitude of 70 km, and the half lower part that for 85 km. In addition,  $X$  and  $Y$  are the distance  $x$  and  $y$  normalized by the radius  $R$  of the reference circular cylinder. Also, it should be emphasized that the density scale is common for all of the cases, even though the scale for the coordinate axis is different.

By examining the density contours depicted in Figs. (4a), (4b) and (4c), it is observed that the major changes in density occur in a thin region close to the body surface. As mentioned earlier, the pick in density occurs at the stagnation point, and the higher value is attained for the bluntest leading edge investigated, the leading edge corresponding to  $n$  of 1/2. As the altitude increases, a reduction on the density level is observed not only at the stagnation point but also adjacent to the body surface.

Also of great significance in Figs. (4a), (4b) and (4c) is the disturbance domain upstream the nose of the leading edges. Similar to the velocity profiles, the density disturbance is more pronounced for the bluntest leading edge investigated. Also it is clearly noticed that the upstream effect increases with the altitude rise, as was pointed previously.

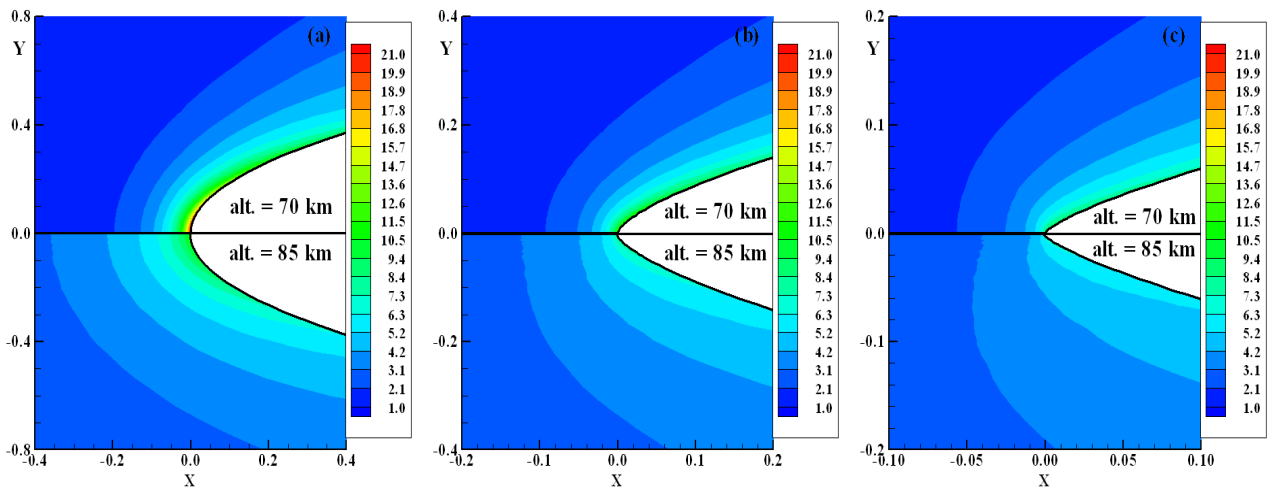


Figure 4: Density ratio ( $\rho/\rho_\infty$ ) contours at the vicinity of the leading-edge nose as a function of the altitude for leading-edge shapes that correspond to the power-law exponents of (a) 1/2, (b) 2/3 and (c) 3/4.

### 4.3. Pressure Profile

The large amount of kinetic energy present in a hypersonic freestream is converted by molecular collisions into high thermal energy surrounding the body and by flow work into increased pressure. In this respect, the stagnation line is a zone of strong compression, where pressure increases from the freestream to the stagnation point due to the shock wave that forms ahead of the leading edges.

Variations on pressure profiles along the stagnation streamline due to rarefaction effect are displayed as a function of the altitude in Figs. (5a), (5b) and (5c) for power-law exponent  $n$  of 1/2, 2/3 and 3/4, respectively. In this set of diagrams, pressure  $p$  is normalized by the freestream pressure  $p_\infty$ . The general shape of the dimensionless pressure profile is preserved even for the highest altitude investigated. In this fashion, the pressure increases from the freestream value toward the stagnation point where the maximum value is attained. The maximum pressure located at the stagnation point decreases with the altitude rise. Also, it decreases as the power-law exponent  $n$  increases, since the leading edge becomes sharp. At the stagnation region, the compression produces a maximum pressure that is around two order of magnitude higher than the freestream value for the cases investigated.

The extent of the upstream flowfield disturbance for pressure is significantly different from that presented by density. The domain of influence for pressure is higher than that for density and lower than that presented for temperature. Similar to the density, much of the pressure increase in the shock layer occurs after the translational kinetic temperature has reached its postshock value, as will be shown subsequently.

In what follows, a critical assessment of the flowfield is provided by Figs. (6a), (6b) and (6c) which consider a magnification of the pressure ratio,  $p/p_\infty$  at the vicinity of the leading edge for power-law exponent of 1/2, 2/3 and 3/4, respectively.

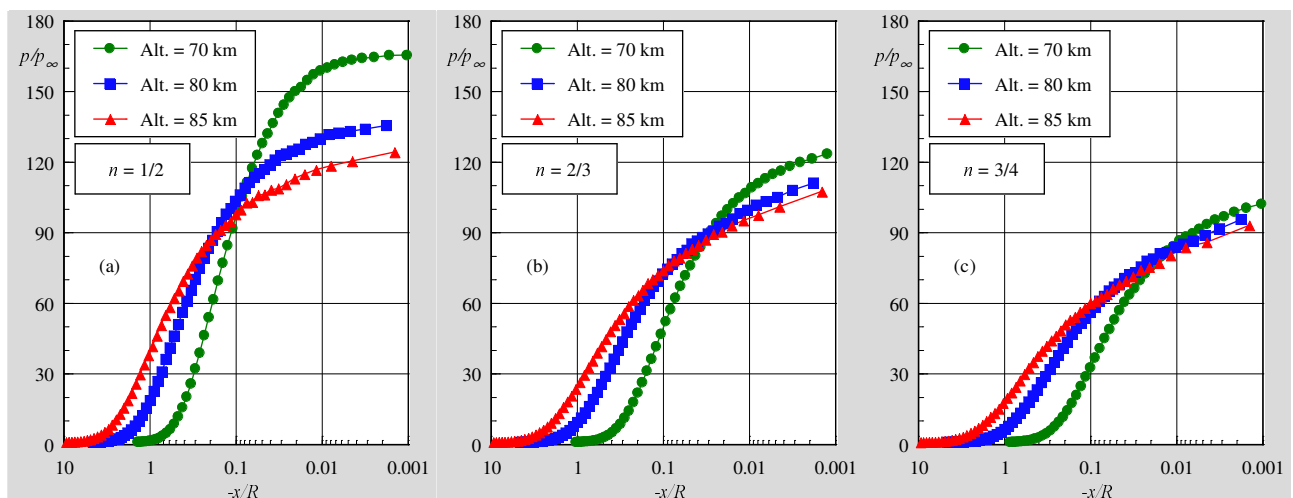


Figure 5: Pressure ( $p/p_\infty$ ) profiles along the stagnation streamline as a function of the altitude for leading-edge shape corresponding to power-law exponent  $n$  of (a) 1/2, (b) 2/3 and (c) 3/4.

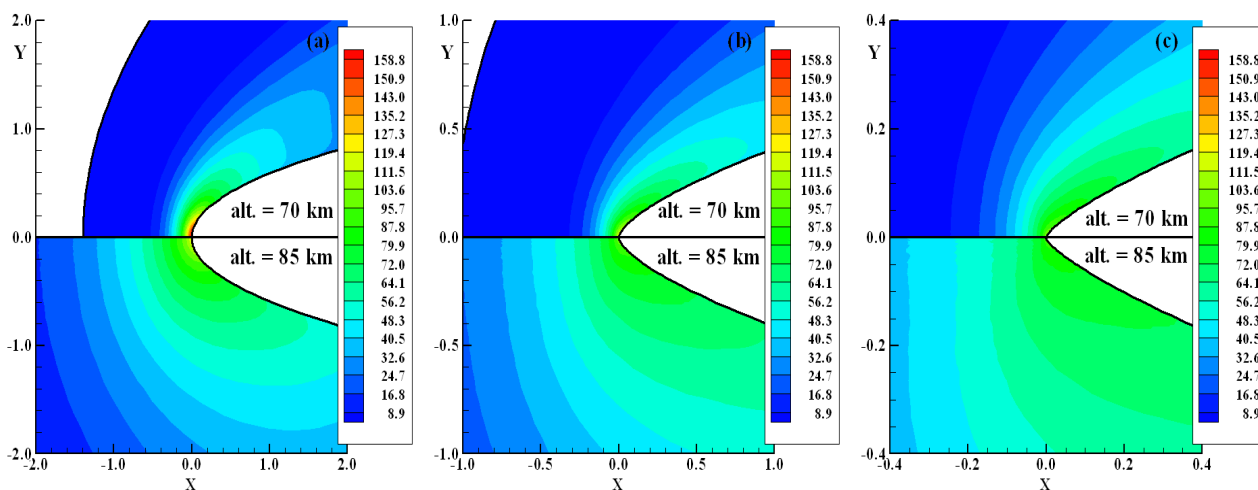


Figure 6: Pressure ratio ( $p/p_\infty$ ) contours at the vicinity of the leading-edge nose as a function of the altitude for leading-edge shapes that correspond to the power-law exponents of (a) 1/2, (b) 2/3 and (c) 3/4.

Referring to Figs. (6a), (6b) and (6c), it is clearly observed that the stagnation region is a zone of strong compression. Moreover, due to the expansion along the body surface, the pressure adjacent to the surface presents a significant reduction as compared to the freestream pressure.

#### 4.4. Temperature Profile

The strong shock wave that forms ahead of a blunt leading edge at hypersonic flow converts part of the kinetic energy of the freestream air molecules into thermal energy. This thermal energy downstream of the shock wave is partitioned into increasing the translational kinetic energy of the air molecules, and into exciting of other molecular energy states such as rotation and vibration.

Kinetic temperature profiles along the stagnation streamline are demonstrated as a function of the altitude in Figs. (7), (8) and (9) for power-law exponent  $n$  of 1/2, 2/3 and 3/4, respectively. In this set of plots, temperature ratio accounts for the kinetic temperatures normalized by the freestream temperature  $T_\infty$ . In addition,  $T_T$ ,  $T_R$ ,  $T_V$  and  $T_O$  stand for translational, rotational, vibrational and overall temperature, respectively. It is apparent from these figures that thermodynamic non-equilibrium occurs throughout the shock layer, as shown by the lack of equilibrium of the translational and internal kinetic temperatures. Thermal non-equilibrium occurs when the temperatures associated with the translational, rotational, and vibrational modes of a polyatomic gas are different.

The overall kinetic temperature shown is defined for a non-equilibrium gas as the weighted mean of the translational and internal temperature (Bird, 1994) as follows,

$$T = \frac{\zeta_T T_T + \zeta_R T_R + \zeta_V T_V}{\zeta_T + \zeta_R + \zeta_V} \quad (2)$$

where  $\zeta$  is the degree of freedom, and subscripts  $T$ ,  $R$  and  $V$  stand for translational, rotational and vibrational modes.

The overall kinetic temperature is equivalent to the thermodynamic temperature only under thermal equilibrium conditions. It is important to mention that the ideal gas equation of state does not apply to this temperature in a non-equilibrium situation.

Referring to Figs. (7), (8) and (9), in the undisturbed freestream far from the body, the translational and internal temperatures have the same value and are equal to the thermodynamic temperature. Approaching the nose of the leading edge, the translational temperature rises to well above the rotational and vibrational temperatures and reaches a maximum value that is a function of the leading edge shape as well as of the altitude. Since a large number of collisions is needed to excite molecules vibrationally from the ground state to the upper state, the vibrational temperature increases much more slowly than rotational temperature. Still further downstream toward the nose of the leading edge, the translational temperature decreases and reaches a value on the wall that is above the wall temperature, resulting in a temperature jump as defined in continuum formulation.

It is evident by comparison with Fig. (3) that, for the altitudes investigated, the translational kinetic temperature rises to a peak well before any substantial increase in density has been experienced. This rise is due to the particles being reflected forward from the compression region into the low-density approaching flow. Energetic collisions between the fast moving freestream particles and reflected ones result in the translational kinetic temperature rising to a peak comparable in magnitude to that behind the bow shock for the equivalent continuum flow.

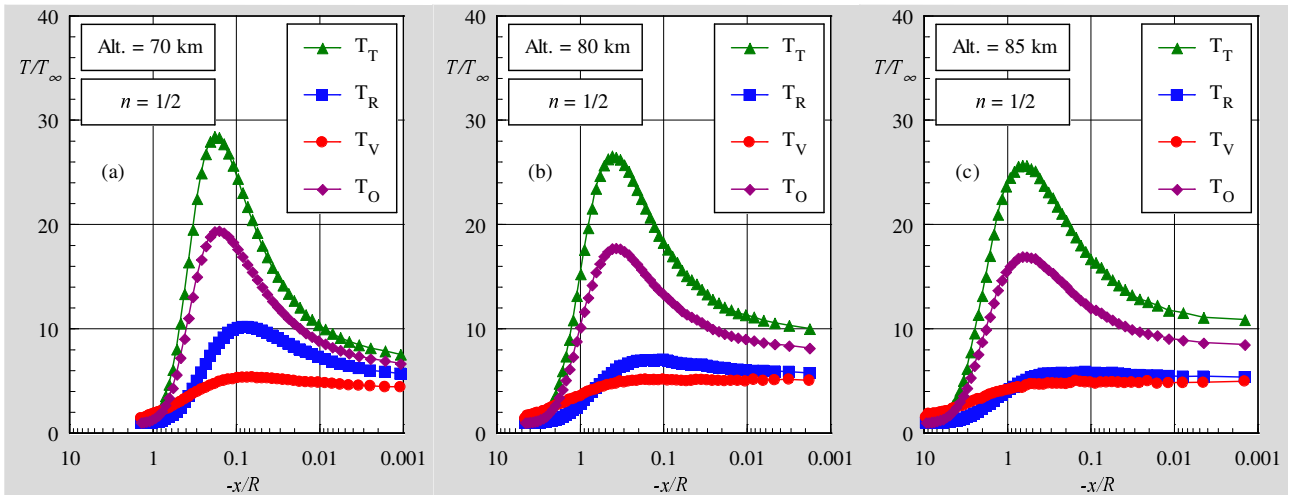


Figure 7: Kinetic temperature ( $T/T_\infty$ ) profiles along the stagnation streamline for leading-edge shape that corresponds to the power-law exponent of  $1/2$  for altitudes of (a) 70, (b) 80 and (c) 85 km.

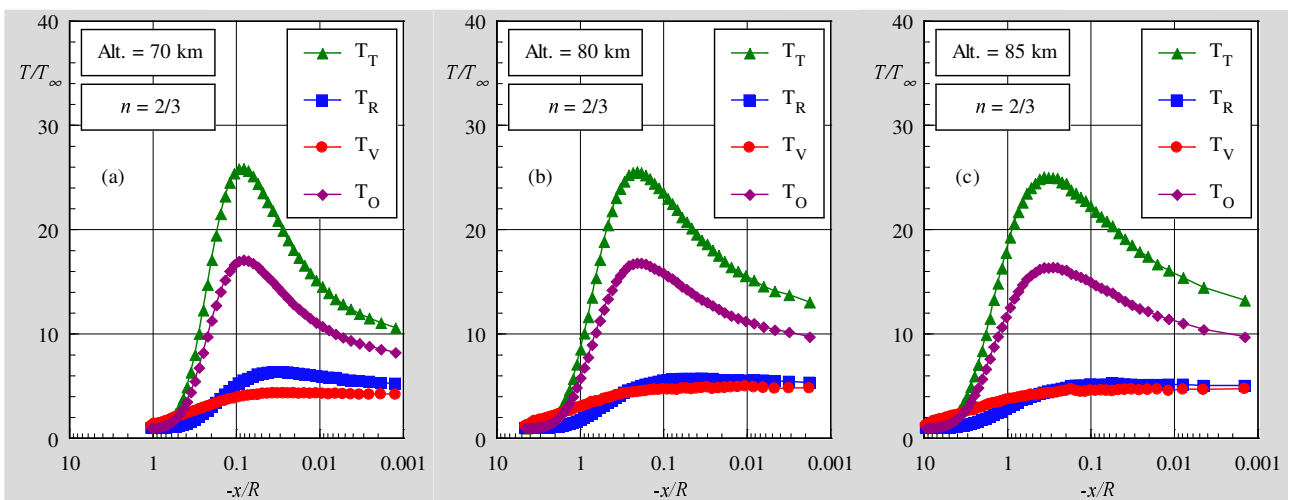


Figure 8: Kinetic temperature ( $T/T_\infty$ ) profiles along the stagnation streamline for leading-edge shape that corresponds to the power-law exponent of  $2/3$  for altitudes of (a) 70, (b) 80 and (c) 85 km.

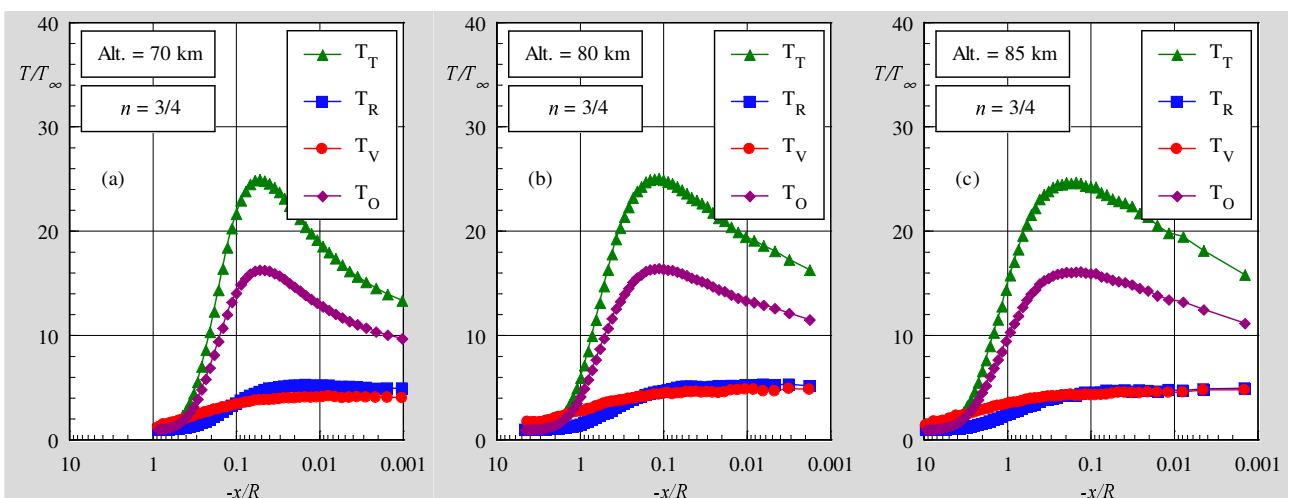


Figure 9: Kinetic temperature ( $T/T_\infty$ ) profiles along the stagnation streamline for leading-edge shape that corresponds to the power-law exponent of  $3/4$  for altitudes of (a) 70, (b) 80 and (c) 85 km.

The magnitude of the peak for the translational temperature is higher for altitude of 70 km than those for altitudes of 80 and 85 km, since the freestream temperature  $T_\infty$  corresponds to 220, 181 and 181 K, for altitudes of 70, 80 and 85 km, respectively. Although the freestream Knudsen number increases around 2.5 times as the altitude increases from 80 to 85 km, very little variation in the translational kinetic temperature peak is seen.

As the density of a flow is reduced from that of continuum conditions, the conditions of temperature continuity adjacent to the body surface are no longer satisfied. This occurs because the state of the molecules adjacent to the body surface is affected not only by the surface but also by the flow conditions at a distance of the order of a mean free path from the surface. Consequently, as the flow becomes more rarefied, the spatial region, which influences the state of the gas adjacent to the body surface, increases and gives rise to a significant temperature jump effect. This effect is more pronounced as the altitude is increased, as shown in Fig. (9). It is worth noting that the wall temperature ratio  $T_w/T_\infty$  corresponds to 4.0 for altitude of 70 km and 4.8 for altitudes of 80 and 85 km.

In an effort to provide additional information concerning the flowfield structure, dimensionless overall temperature contours on color maps are illustrated in Fig. (10). This set of plots clearly illustrates the effect of the leading-edge shapes as well as the effect of rarefaction on the flowfield structure.

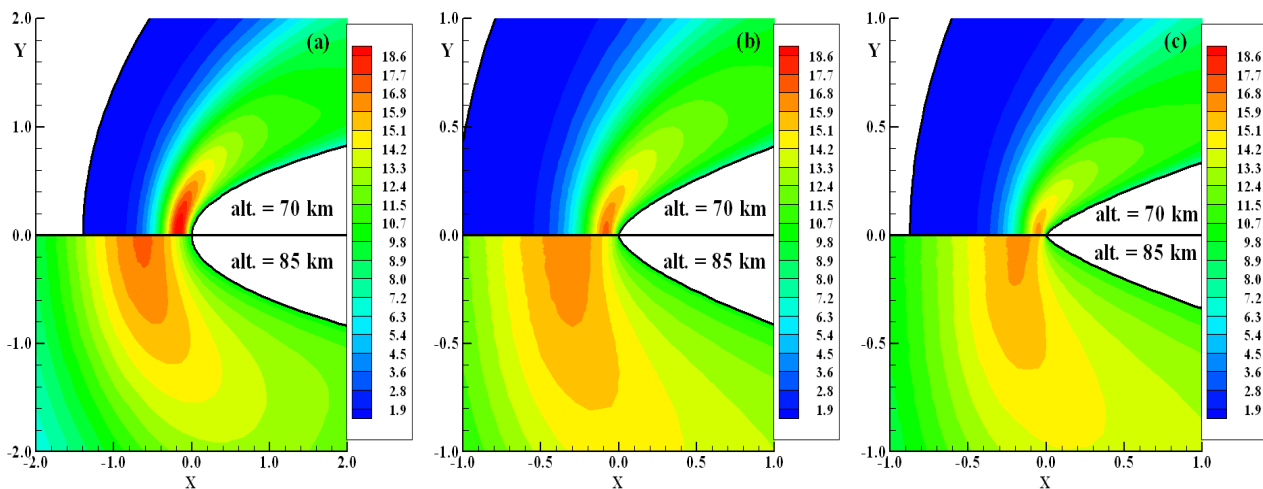


Figure 10: Overall temperature ( $T_o/T_\infty$ ) contours at the vicinity of the leading-edge nose as a function of the altitude for leading-edge shapes that correspond to the power-law exponents of (a) 1/2, (b) 2/3 and (c) 3/4.

## 5. Concluding Remarks

Computations of a rarefied hypersonic flow on power-law shaped leading edges have been performed by using the Direct Simulation Monte Carlo method. The calculations provided information concerning the nature of the flowfield structure about the primary flow properties at the vicinity of the nose and immediately adjacent to the body surface.

Effects of rarefaction on the velocity, density, pressure, and temperature for a wide range of parameters were investigated. The altitude varied from 70 to 85 km, which correspond to an increase of one order of magnitude on the freestream mean free path. In addition to that, the power-law exponent ranged from 1/2 to 3/4, corresponding blunt and sharp power-law leading edges. Cases considered in this study covered the hypersonic flow on the transitional flow regime.

It was found that changes on the altitude as well as on the shape of the leading edge disturbed the flowfield far upstream, as compared to the radius of the reference circular cylinder, and the domain of influence increased with increasing the altitude, and decreased by increasing the power-law exponent, as the leading edge became sharp. Moreover, the extent of the upstream flowfield disturbance is significantly different for each one of the primary flow properties. The domain of influence for temperature is larger than that observed for pressure and density. Since the extent of the flowfield disturbance is significantly different for each one of the leading edge shapes, this will have important implications in problems that take into account for the gas-phase chemistry and for the gas-surface catalytic activity.

## 6. References

- Alexander, F. J., Garcia, A. L., and, Alder, B. J., 1998, "Cell Size Dependence of Transport Coefficient in Stochastic Particle Algorithms", *Physics of Fluids*, Vol. 10, No. 6, pp. 1540-1542.
- Alexander, F. J., Garcia, A. L., and, Alder, B. J., 2000, "Erratum: Cell Size Dependence of Transport Coefficient is Stochastic Particle Algorithms", *Physics of Fluids*, Vol. 12, No. 3, pp. 731-731.

- Anderson, J. L., 1990, "Tethered Aerothermodynamic Research for Hypersonic Waveriders", Proceedings of the 1st International Hypersonic Waverider Symposium, Univ. of Maryland, College Park, MD.
- Bird, G. A., 1981, "Monte Carlo Simulation in an Engineering Context", Progress in Astronautics and Aeronautics: Rarefied gas Dynamics, Ed. Sam S. Fisher, Vol. 74, part I, AIAA New York, pp. 239-255.
- Bird, G. A., 1989, "Perception of Numerical Method in Rarefied Gasdynamics", Rarefied gas Dynamics: Theoretical and Computational Techniques, Eds. E. P. Muntz, and D. P. Weaver and D. H. Capbell, Vol. 118, Progress in Astronautics and Aeronautics, AIAA, New York, pp. 374-395.
- Bird, G. A., 1994, "Molecular Gas Dynamics and the Direct Simulation of Gas Flows", Oxford University Press, Oxford, England, UK.
- Borgnakke, C. and Larsen, P. S., 1975, "Statistical Collision Model for Monte Carlo Simulation of Polyatomic Gas Mixture", Journal of computational Physics, Vol. 18, No. 4, pp. 405-420.
- Garcia, A. L., and, Wagner, W., 2000, "Time Step Truncation Error in Direct Simulation Monte Carlo", Physics of Fluids, Vol. 12, No. 10, 2000, pp. 2621-2633.
- Graves, R. E. and Argrow, B. M., 2001, "Aerodynamic Performance of an Osculating-Cone Waverider at High Altitudes", Proceedings of the 35th AIAA Thermophysics Conference, AIAA Paper 2001-2960, Anaheim, CA.
- Guo, K. and Liaw, G.-S., 2001, "A Review: Boundary Conditions for the DSMC Method", Proceedings of the 35th AIAA Thermophysics Conference, AIAA Paper 2001-2953, Anaheim, CA, 11-14 June.
- Haas, B. L., Fallavollita, M. A., 1994, "Flow Resolution and Domain Influence in Rarefied Hypersonic Blunt-Body Flows", Journal of Thermophysics and Heat Transfer, Vol. 8, No. 4, pp. 751-757.
- Hadjiconstantinou, N. G., 2000, "Analysis of Discretization in the Direct Simulation Monte Carlo", Physics of Fluids, Vol. 12, No. 10, pp. 2634-2638.
- Mason, W. H. and Lee, J., 1994, "Aerodynamically Blunt and Sharp Bodies", Journal of Spacecraft and Rockets, Vol. 31, No. 3, pp. 378-382.
- Nonweiler, T. R. F., 1959, "Aerodynamic Problems of Manned Space Vehicles", Journal of the Royal Aeronautical Society, Vol. 63, Sept, pp. 521-528.
- Potter, J. L. and Rockaway, J. K., 1994, "Aerodynamic Optimization for Hypersonic Flight at Very High Altitudes", Rarefied gas Dynamics: Space Science and Engineering, eds. B. D. Shizgal and D. P. Weaver, vol. 160, pp. 296-307, Progress in Astronautics and Aeronautics, AIAA New York.
- Rault, D. F. G., 1994, "Aerodynamic Characteristics of a Hypersonic Viscous Optimized Waverider at High Altitude", Journal of Spacecraft and Rockets, Vol. 31, No. 5, pp. 719-727.
- Santos, W. F. N. and Lewis, M. J., 2002, "Power Law Shaped Leading Edges in Rarefied Hypersonic Flow", Journal of Spacecraft and Rockets, Vol. 39, No. 6, pp. 917-925.
- Santos, W. F. N. and Lewis, M. J., 2005a, "Aerothermodynamic Performance Analysis of Hypersonic Flow on Power Law Leading Edges", Journal of Spacecraft and Rockets, Vol. 42, No. 4, pp. 588-597.
- Santos, W. F. N. and Lewis, M. J., 2005b, "Calculation of Shock Wave Structure over Power Law Bodies in Hypersonic Flow", Journal of Spacecraft and Rockets, Vol. 42, No. 2, pp. 213-222.
- Shvets, A. I., Voronin, V. I., Blankson, I. M., Khikine, V., & Thomas, L., 2005, "On Waverider Performance with Hypersonic Flight Speed and High Altitudes", Proceedings of the 43rd AIAA Aerospace Sciences Meeting and Exhibit, AIAA Paper 2005-0512, Reno, NV.